ACS NANO
Cite This: ACS Nano 2018, 12, 12869−12878
www.acsnano.org

ARTICLE

Layered-Structure $SbPO_4$/Reduced Graphene Oxide: An Advanced Anode Material for Sodium Ion Batteries

Jun Pan,[†,⊥] Shulin Chen,[‡,¶,⊥] Qiang Fu,[†] Yuanwei Sun,[‡] Yuchen Zhang,[†] Na Lin,[§] Peng Gao,[*,‡,#] Jian Yang,[*,†] and Yitai Qian[†,∥]

[†]Key Laboratory of Colloid and Interface Chemistry Ministry of Education School of Chemistry and Chemical Engineering, Shandong University, Jinan 250100, P.R. China

[‡]International Center for Quantum Materials, and Electron Microscopy Laboratory, School of Physics, Peking University, Beijing 100871, P.R. China

[¶]State Key Laboratory of Advanced Welding and Joining, Harbin Institute of Technology, Harbin 150001, China

[§]State Key Lab of Crystal Materials, Shandong University, Jinan 250100, P.R. China

[#]Collaborative Innovation Center of Quantum Matter, Beijing 100871, China

[∥]Hefei National Laboratory for Physical Science at Microscale, Department of Chemistry, University of Science and Technology of China, Hefei 230026, P.R. China

Supporting Information

ABSTRACT: **Sodium ion batteries are one of most promising alternatives to lithium ion batteries for large-scale energy storage, due to the high abundance and low cost of sodium in the earth. However, the lack of advanced electrode materials greatly affects their applications. Here, layered-structure $SbPO_4$ is explored as an anode material for sodium ion batteries in terms of $SbPO_4$ nanorods on reduced graphene oxide ($SbPO_4$/rGO). *In situ* transmission electron microscopy images reveal the preferential expansion along the transverse direction of the nanorods upon the first discharging, which arises from the reduction of $SbPO_4$ to Sb and the subsequent alloying of Sb as supported by *in situ* X-ray diffraction and selected area electron diffraction patterns. $SbPO_4$/rGO exhibits a capacity retention of 99% after 100 cycles at 0.5 A g^{-1} both in half cells and in full cells. Its specific capacity at 5 A g^{-1} is 214 mA h g^{-1} in half cells or 134 mA h g^{-1} in full cells. Moreover, the energy density of the full cells at 1.2 kW kg^{-1}_{total} is still 99.8 W h kg^{-1}_{total}, very promising as an advanced electrode material.**

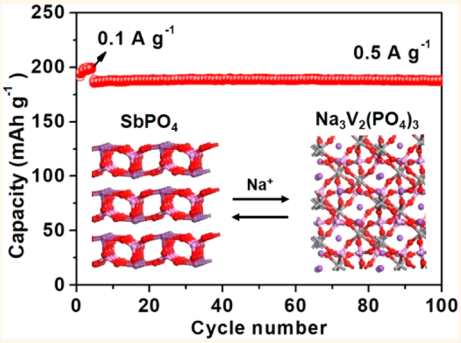

KEYWORDS: *layered structure, antimony, phosphate, anode, sodium ion batteries*

Lithium ion batteries (LIBs), as high-efficiency energy storage devices, have achieved great successes in the past decades.[1,2] However, the limited resources of lithium, especially those available for exploitation, make the prospect of LIBs dim. Thus, sodium ion batteries (NIBs) are developed to address this concern and so far have attracted extensive attention.[3,4] Although NIBs share the same cell configuration as that in LIBs, the electrode materials have to be re-explored because the larger diameter and heavier mass of Na^+ compared to those of Li^+ significantly degrade the electrochemical performances.[5] Meanwhile, Na is chemically more active than Li, triggering more side reactions with electrolytes.[6] Therefore, seeking suitable electrode materials for NIBs is very challenging. Graphite, the commercialized anode material in LIBs, is not a good candidate for NIBs[7] because its interlayer spacing is too small for Na^+. Meanwhile, the small capacity and low initial Coulombic efficiency also impede its practical applications. Transition metal oxides do not work either, due to their large volume changes upon cycling and high working voltages (1−2 V).[8,9] Recently, phosphorus has been indicated as an anode material for NIBs,[10] due to its high theoretical capacity and low working voltage. However, large-scale processing of phosphorus may be dangerous because it can easily transform to highly flammable and toxic allotropes. Meanwhile, the composite of phosphorus/carbon further increases the fire risk.

Received: October 22, 2018
Accepted: November 19, 2018
Published: November 19, 2018

DOI: 10.1021/acsnano.8b08065
ACS Nano 2018, 12, 12869−12878

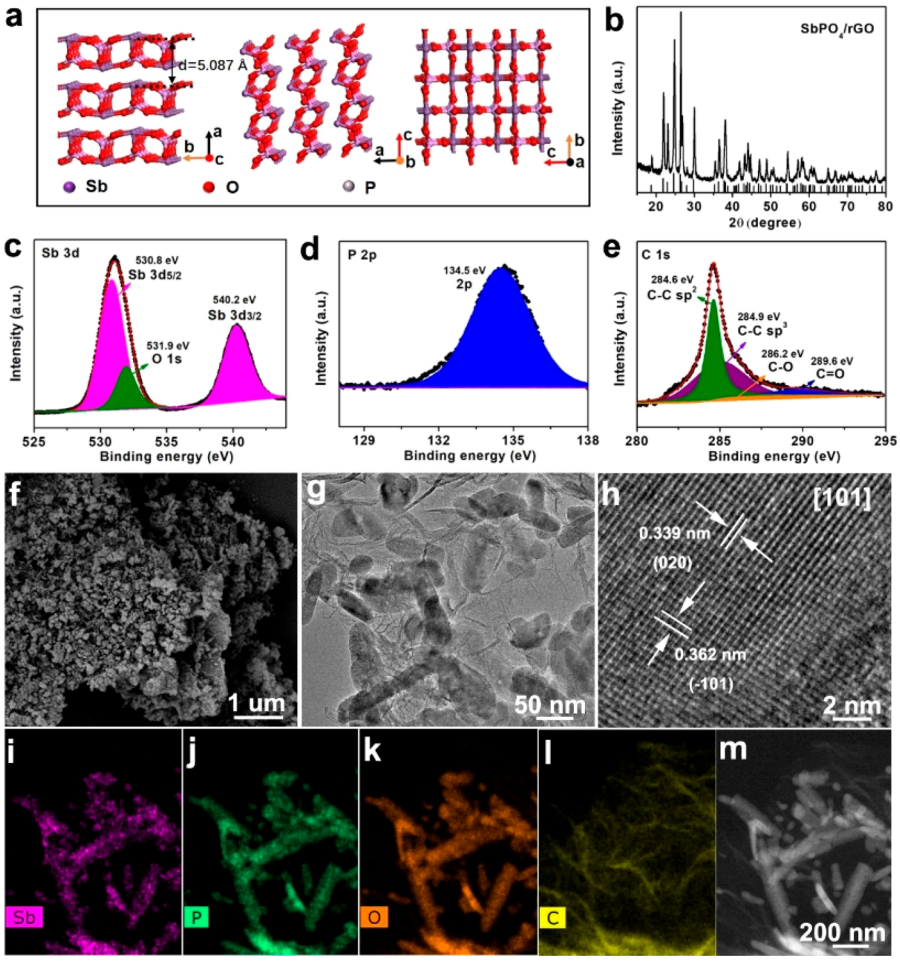

Figure 1. Crystal structure and morphology of $SbPO_4$/rGO. (a) Crystal structure of $SbPO_4$. (b) XRD pattern, (c–e) XPS spectra, (f) FE-SEM, (g) TEM image, (h) HRTEM image, (i–l) element maps of Sb, P, O, and C, and (m) corresponding HAADF-STEM image.

Compared to other candidates, anode materials based on alloying reactions always show high theoretical capacities. The typical examples include, but are not limited to, Sb, Sb_2S_3, Sn, SnO_2, SnS_x, and so on.[11−14] However, these materials are often subjected to substantial volume changes and large structure strain/stress upon cycling, which can easily induce structure deconstruction, particle pulverization, and thus performance degradation. In this context, how to maintain the structure upon cycling becomes the priority. Moreover, Na_2O and Na_2S generated in discharged electrodes are poorly conductive. Na_2S is likely to be oxidized to polysulfides, followed by dissolving into electrolytes.[15] Compared to oxides and sulfides, phosphates have received much less attention[16−18] but do show promising potential as anode materials. First, bulky and stable PO_4^{3-} anions can cushion the volume change upon cycling, thus promoting the cycling stability. Although Na_2O and Na_2S *in situ* generated during the sodiation process may have the similar effect, the enhancement is not comparable to Na_3PO_4 in theory. Meanwhile, Na_3PO_4 generated by the discharge reaction was reported to be an ionic conductor.[19] Therefore, it may reduce the diffusion barrier of Na^+ and promote the reaction kinetics. Second, Sb, Na_xSb, Sn, or Na_xSn generated during the sodiation process can lead to three-dimensional electron pathways because they are either metals or intermetallics.[20,21] Third, phosphates have a variety of crystal structures that are electrochemically active, such as layered structure ($SbPO_4$), NASICON structure ($NaSn_2(PO_4)_3$), *etc.*[15,17,18] Because the structure of electrode materials has a significant effect on the electrochemical performances, the test of phosphates in different structures is necessary and important. All of these features together make the exploration on phosphates attractive.

Here, monoclinic-phase $SbPO_4$ is developed as the target material to illustrate the promising potential of phosphates in NIBs. In this phase, PO_4 and SbO_4 tetrahedra connect together at the corners, resulting in a layered structure (Figure 1a). These layers stack along *a*-axis with an interlayer spacing of 5.087 Å. In order to improve the electrochemical performances of $SbPO_4$, it is deposited to reduced graphene oxide (rGO) by a simple process, denoted as $SbPO_4$/rGO. *Ex situ* characterization techniques, such as high-resolution transmission electron microscope (HRTEM) images and selected area electron diffraction (SAED) patterns, and *in situ* characterization techniques, such as X-ray diffraction (XRD), transmission electron microscopy (TEM), and SAED are measured to reveal the electrochemical reactions and morphology change of this composite upon cycling. Meanwhile, the electrochemical performances of $SbPO_4$/rGO are evaluated both in half cells and in full cells. It presents an excellent cycling stability, with 99% capacity retention after 100 cycles at 0.5 A g^{-1}. The full cells paired with homemade $Na_3V_2(PO_4)_3$/C give a high output voltage at 2.6 V, resulting in an energy density of 99.8 W h kg^{-1}_{total} at 1.2 kW kg^{-1}_{total}. As an anode material, these data make it very attractive in the future.

DOI: 10.1021/acsnano.8b08065
ACS Nano 2018, 12, 12869−12878

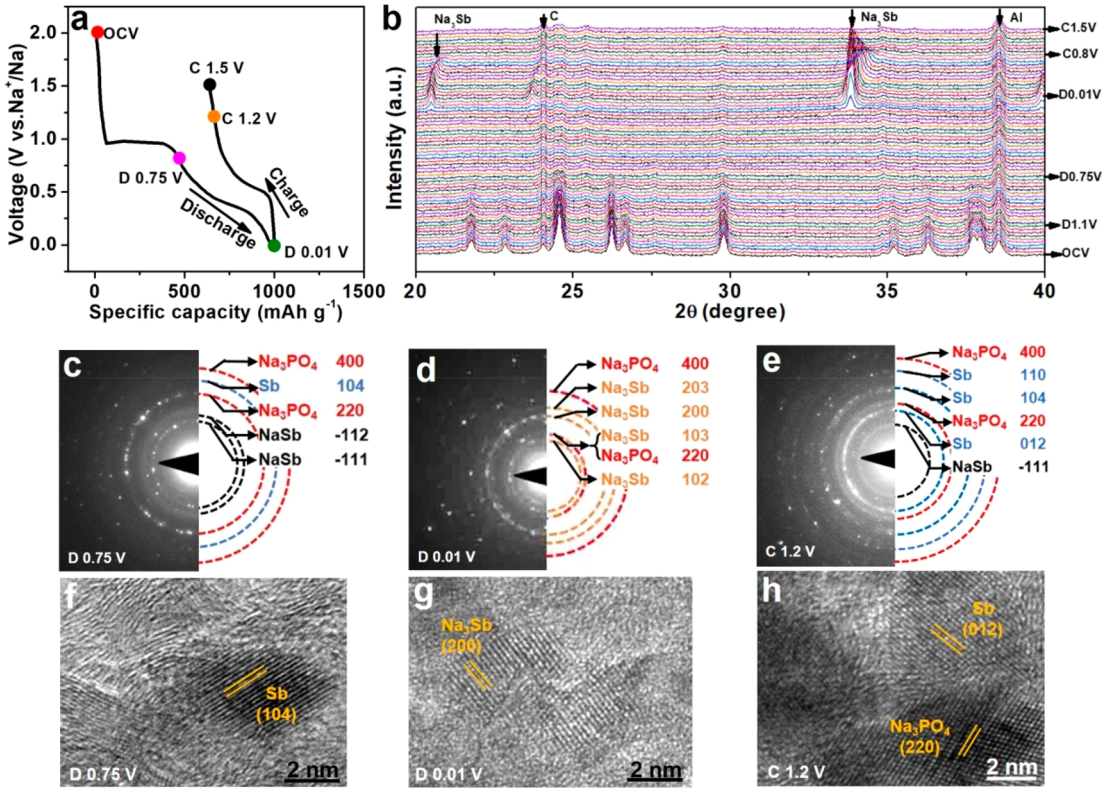

Figure 2. Evolution of $SbPO_4$/rGO during the sodiation/desodiation processes. (a) Galvanostatic discharge/charge profiles at the first cycle. (b) *In situ* XRD patterns, (c–e) *ex situ* SAED patterns, and (f–h) HRTEM images at different states of discharge/charge.

RESULTS AND DISCUSSION

$SbPO_4$/rGO was synthesized by a solvothermal reaction between $SbCl_3$ and $NH_4H_2PO_4$ in the presence of GO, followed by an annealing in Ar/H_2 (see the Experimental Section). Figure 1b shows the XRD pattern of the resultant product, where all the diffraction peaks could be indexed as monoclinic-phase $SbPO_4$ (JCPDS Card No. 35-0829). No diffraction peaks or bumps assigned to GO or rGO can be observed, probably due to the low contents and/or poor crystallinity. To clarify this point, Raman spectra (Figure S1) were measured, where two peaks at ~1435 and ~1580 cm^{-1} assigned to the D-band and the G-band of carbon are readily observed.[22] It is believed that GO is reduced to rGO during the synthesis, due to the annealing in Ar/H_2 at a high temperature. Such a reduction is directly confirmed by Fourier transform infrared spectra (Figure S2). In this context, the final product is denoted as $SbPO_4$/rGO. Thermogravimetric analysis (TGA) (Figures S3 and S4) shows that the content of rGO in $SbPO_4$/rGO is approximately ~14.3 wt %. X-ray photoelectron spectroscopy (XPS) was conducted to reveal the surface species of $SbPO_4$/rGO. The signals of Sb, P, O, and C could be easily observed in the survey spectrum (Figure S5). The high-resolution spectra of these elements confirm the formation of $SbPO_4$/rGO. As illustrated in Figure 1c, the peaks at 530.8 and 540.2 eV are assigned to Sb $3d_{5/2}$ and Sb $3d_{3/2}$ of $SbPO_4$, and the peak at 531.9 eV is ascribed to O 1s.[23] The similar overlapping between Sb 3d and O 1s has been reported in previous works.[24] The peak at 134.5 eV in Figure 1d is assigned to P 2p from P–O in PO_4^{3-}.[25] Different from the spectra of P 2p and Sb 3d, there are four peaks in the C 1s spectra (Figure 1e), which are 284.6 eV from sp^2-bonded C–C, 284.9 eV from sp^3-bonded C–C, 286.2 eV from C–O, and 289.6 eV from O=C–OH.[26] The presence of C–O, C=O, and O=C–OH offers numerous anchoring sites for electrochemically active materials and then inhibits particle agglomeration or drop-off from electrodes.

Then, $SbPO_4$/rGO was characterized by field-emission scanning electron microscopy (FE-SEM) and TEM. Figure 1f shows that numerous nanoparticles are well dispersed on a sheet-like structure, indicating the formation of $SbPO_4$/rGO. The high-magnification TEM image (Figure 1g) reveals that there are many short nanorods, with a diameter of 50 nm and length up to 350 nm. It is also noted that there is a small quantity of ellipsoids in $SbPO_4$/rGO. The high-resolution TEM (HRTEM) image on a single nanorod (Figure 1h) exhibits clear lattice fringes throughout the entire nanorod, indicating a single-crystal nature. The fringes with their interlayer spacings at 0.339 and 0.362 nm correspond to (020) and (−101) planes of $SbPO_4$, respectively. The fast Fourier transform pattern, as shown in Figure S6, suggests that the nanorods grow along the direction of [−101], parallel to the polyhedron layers of $SbPO_4$. Energy-dispersive X-ray spectra (EDS) (Figure S7) confirm the molar ratio of Sb to P at almost 1:1, close to that in $SbPO_4$. To figure out the distributions of these elements, high-angle annular dark-field scanning TEM (HAADF-STEM) images and element mapping were conducted. As presented in Figure 1i–m, the patterns of Sb, P, and O are well overlapped with that of nanorods, strongly supporting the formation of $SbPO_4$ nanorods. Meanwhile, the signal of carbon from rGO is also observed in Figure 1l. All of these results confirm that $SbPO_4$ nanorods are attached to rGO. This good contact would benefit the charge transfer between rGO and $SbPO_4$ and restrain the particle pulverization upon cycling, thereby improving rate

DOI: 10.1021/acsnano.8b08065
ACS Nano 2018, 12, 12869–12878

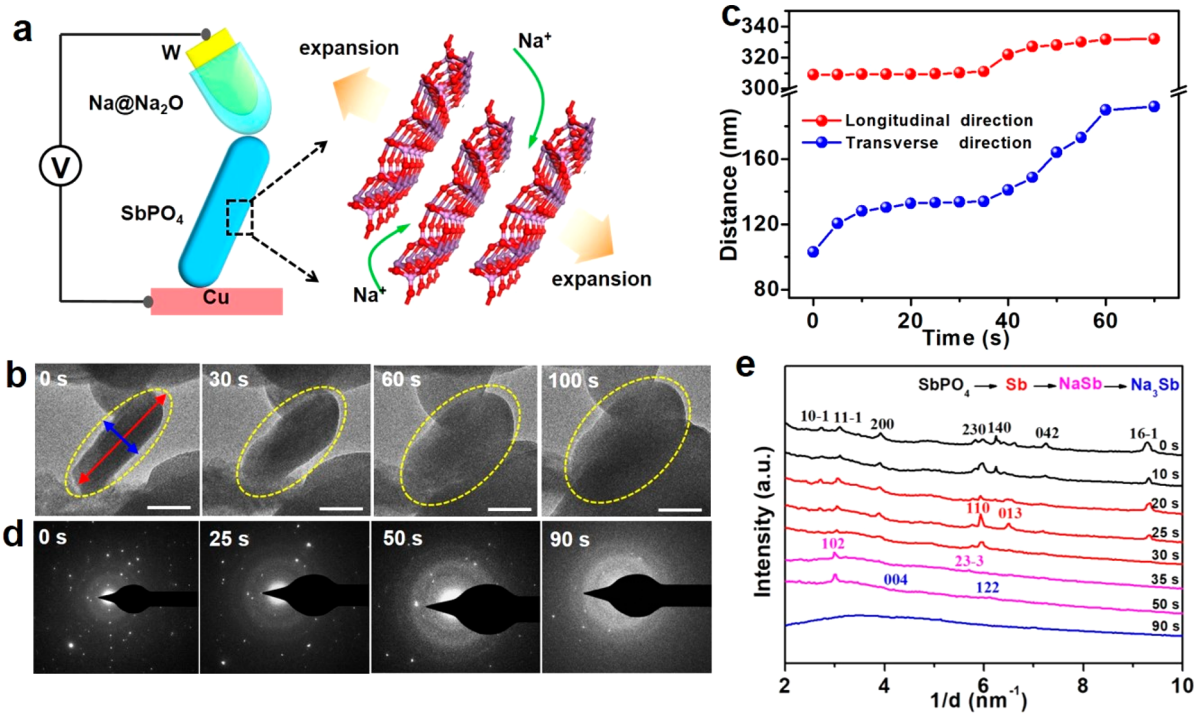

Figure 3. ***In situ*** **TEM imaging of the sodiation process of $SbPO_4$. (a) Schematic illustration on electrochemical setup for** ***in situ*** **TEM imaging, where metallic Na was taken as the counter electrode and a thin layer of Na_xO on Na was used as the solid-state electrolyte. (b) Morphology changes of a single nanorod by** ***in situ*** **TEM. (c) Size changes in the longitudinal and transverse directions over time. (d) Phase evolutions of another nanostructure by** ***in situ*** **SAED pattern. (e) Corresponding radially integrated intensity profiles from a series of time-sequence SAED patterns.**

capability and cycling stability. N_2 sorption isotherms (Figure S8) suggest that $SbPO_4$/rGO has a specific surface area of about 50.8 m^2 g^{-1} and an average pore size of about 30 nm.

Figure 2a shows the discharge/charge profiles of $SbPO_4$ at the first cycle. There is a pronounced voltage plateau at 0.9 V, indicating a typical two-phase process. After that, the voltage profile is followed by a shallow slope over 0.6−0.25 V. Compared to the discharge profile, only one short voltage slope between 0.5 and 0.75 V is observed in the first charge. In view of specific capacity and average voltage, it is believed that this voltage slope corresponds to the reverse reaction that happens over 0.5−0.3 V in the first discharge. To identify these electrochemical reactions, *in situ* XRD patterns and *ex situ* HRTEM images/SAED patterns are measured. As shown in Figure 2b, the diffraction peaks at 24 and 38.5° can be attributed to conductive carbon and the current foil, Al, which do not alter in intensity and in peak positions upon cycling. Different from the cases of C and Al, the diffraction peaks of $SbPO_4$ gradually weaken with discharging and almost disappear below 0.8 V. This result can be speculated as the reduction reaction from $SbPO_4$ to metallic Sb. However, no obvious peaks from metallic Sb and Na_3PO_4 are observed, which is likely caused by their poor crystallinity/small size. The similar phenomenon is very common in the products from conversion reactions.[14,26,27] Although metallic Sb is invisible in XRD patterns, its appearance is confirmed by *ex situ* SAED patterns (Figure 2c) and HRTEM images (Figure 2f), strongly supporting the reduction reaction. As the discharge process proceeds, metallic Sb is alloyed with Na, generating NaSb and Na_3Sb in sequence. At the end of the discharge process, Na_3Sb is easily identified in the XRD patterns (Figure 2b), SAED pattern (Figure 2d), and HRTEM image (Figure 2g). Then, the electrode is charged back, where the diffraction peaks of Na_3Sb shift the high angles and become weak (Figure 2b). This result indicates the contraction of unit cells and the damage of crystal structures. At ∼0.8 V, these diffraction peaks almost disappear from the XRD pattern. Similar to the case of the discharge process, the diffraction peaks from metallic Sb are absent in the XRD pattern, but its diffraction rings and lattice fringes are confirmed by SAED patterns (Figure 2e) and HRTEM images (Figure 2h). This result is kept in the XRD patterns, even as the electrode is charged to 1.5 V (Figure S9). These results confirm that the alloying reaction, rather than the conversion reaction, contributes to the reversible capacity over 0.01−1.5 V, well explaining the low initial Coulombic efficiency of $SbPO_4$. The involved electrochemical reactions upon cycling could be described by eqs 1 and 2:

$$SbPO_4 + 3Na^+ + 3e^- \rightarrow Sb + Na_3PO_4 \quad (1)$$

$$Sb + 3e^- + 3Na^+ \leftrightarrow Na_3Sb \quad (2)$$

As the voltage window is expanded to 0.01−2.5 V, there is one more pair of voltage plateaus, 1.7 V in the discharge process and 2.2 V in the charge process (Figure S10). The HRTEM images and SAED patterns of the electrode charged to 2.5 V (Figure S11) confirm the formation of $SbPO_4$ again. Thus, it is believed that the new voltage plateaus originate from the redox reaction between Sb and $SbPO_4$. However, the capacity contributed by this reaction (∼90 mA h g^{-1}) is much smaller than the expected one (∼366 mA h g^{-1}), indicating that this reaction is partially reversible. The high capacity of $SbPO_4$/rGO over 0.01−2.5 V only lasts for 80 cycles (Figure S12). After that, the capacity decays quickly, due to the larger structure stain/stress caused by the insertion/extraction of

DOI: 10.1021/acsnano.8b08065
ACS Nano 2018, 12, 12869−12878

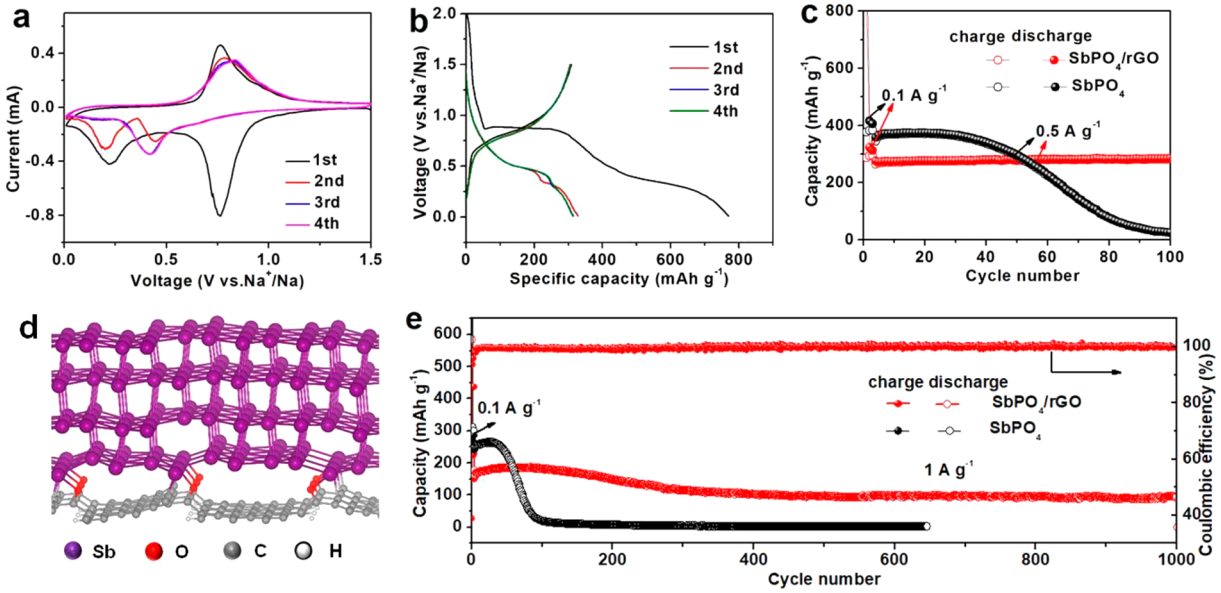

Figure 4. Electrochemical performances of $SbPO_4$/rGO. (a) CV curves. (b) Discharge/charge profiles of $SbPO_4$/rGO at a current density of 0.1 A g^{-1}. (c) Cycling performance. (d) Simulated interface of Sb/rGO. (e) Long cycling performance.

more Na ions. In this regard, the electrochemical test in this work is limited within the voltage window of 0.01−1.5 V.

In situ TEM technique could intuitively reflect the changes of individual electrode particles in morphology and structure with nanometer/atomic resolution.[28,29] Figure 3a shows the configuration of *in situ* TEM imaging, where $SbPO_4$ nanorods and metallic Na were employed as the working electrode and the counter electrode, respectively. The thin layer of Na_xO on Na acted as a solid-state electrolyte, so sodium ions gradually passed through this layer and diffused into $SbPO_4$. Figure 3b shows the real-time TEM images upon discharge, where the nanorod expands anisotropically during sodiation; that is, the length of the $SbPO_4$ nanorod increases slightly (~23 nm) upon discharging, but the diameter expands violently (~90 nm) (Movie S1 and Figure 3c). This anisotropic volume change is likely associated with the unique layered structure of $SbPO_4$ that is aligned along the longitudinal direction of nanorods. Thus, as Na ions diffuse into the interlayers during the sodiation process (right side of Figure 3a), $SbPO_4$ nanorods would preferentially expand along the transverse direction. The *in situ* SAED patterns in Figure 3d were also recorded to track the structural evolution during the discharge process. The diffraction rings are radially integrated to intensity profiles in order to increase the accuracy (Movie S2, Supporting Information). Both the position and intensity of the diffraction peaks vary a lot with the sodiation process, revealing the phase transition from $SbPO_4$ to Sb, NaSb, and eventually to Na_3Sb (Figure 3e). These results disclose the stepwise alloying of Sb during sodiation, in excellent agreement with *ex situ* TEM images.

Figure 4a shows the cyclic voltammetry (CV) curves of $SbPO_4$/rGO during the first four cycles over 0.01−1.5 V at a scan rate of 0.1 mV s^{-1}. In the first cycle, the cathodic peak at 0.75 V is related to the reduction of $SbPO_4$ to metallic Sb, the decomposition of electrolytes, and the formation of a solid electrolyte interphase (SEI) film.[4,30] After that, as-formed Sb alloys with Na, producing a cathodic peak at ~0.25 V, consistent with that reported for this alloying reaction.[31] In the first-charge process, there is only one broad and strong anodic peak at ~0.75 V, which can be attributed to the desodiation of Na_xSb alloy.[32] This result is also in line with those from *in situ* XRD patterns and *in situ* SAED patterns. In the second cycle, the cathodic peak at 0.75 V vanishes, but another peak at 0.4 V shows up, which also originates from the alloying reaction of Sb.[33] The cathodic peak at 0.22 V probably comes from residual Sb that did not react completely during the first discharge. Compared to the changes on the cathodic peaks, that of the anodic peak is quite small. In the third cycle, the cathodic peaks at 0.4 and 0.22 V merge together. From then on, the CV curves become almost identical, implying a good electrochemical stability. Figure 4b shows the discharge/charge profiles of $SbPO_4$/rGO at 0.1 A g^{-1} for the first four cycles. The voltage profiles are in good agreement with the cathodic/anodic peaks in the CV curves. The first discharge/charge capacity is 766/309 mA h g^{-1}, resulting in an initial Coulombic efficiency of 40%. The low Coulombic efficiency comes from irreversible reactions during the first discharging, such as the formation of a SEI film, the irreversible conversion between $SbPO_4$ and metallic Sb, and so on.[34,35] However, after that, the Coulombic efficiency quickly rises to 99.5% and the capacity remains at 306 mA h g^{-1}, very close to the theoretical capacity of this composite (330.4 mA h g^{-1} = 372 mA h g^{-1} × 0.86 + 75 mA h g^{-1} × 0.14) (Figure S13). This result indicates that most of the active material in this composite has been well utilized in a high efficiency. It is noted that the low initial Coulombic efficiency can be improved by presodiation or wide voltage window (Figure S14). Figure 4c displays the cycling performances of $SbPO_4$/rGO and $SbPO_4$ within 0.01−1.5 V, using 1 M $NaClO_4$ in propylene carbonate as the electrolyte. Both of them were activated at 0.1 A g^{-1} for the first three cycles and then cycled at 0.5 A g^{-1}. Apparently, $SbPO_4$/rGO exhibits a much better cycling stability than $SbPO_4$. After 100 cycles at 0.5 A g^{-1}, $SbPO_4$/rGO still delivers a capacity of 280 mA h g^{-1}, much higher than 20 mA h g^{-1} of $SbPO_4$. This result indicates that rGO greatly improves the cycling stability. Unfortunately, the nanorods are not preserved after cycles (Figure S15), probably due to the repeated deformation upon cycling, as illustrated in Figure 3. Despite this, active materials are still

DOI: 10.1021/acsnano.8b08065
ACS Nano 2018, 12, 12869−12878

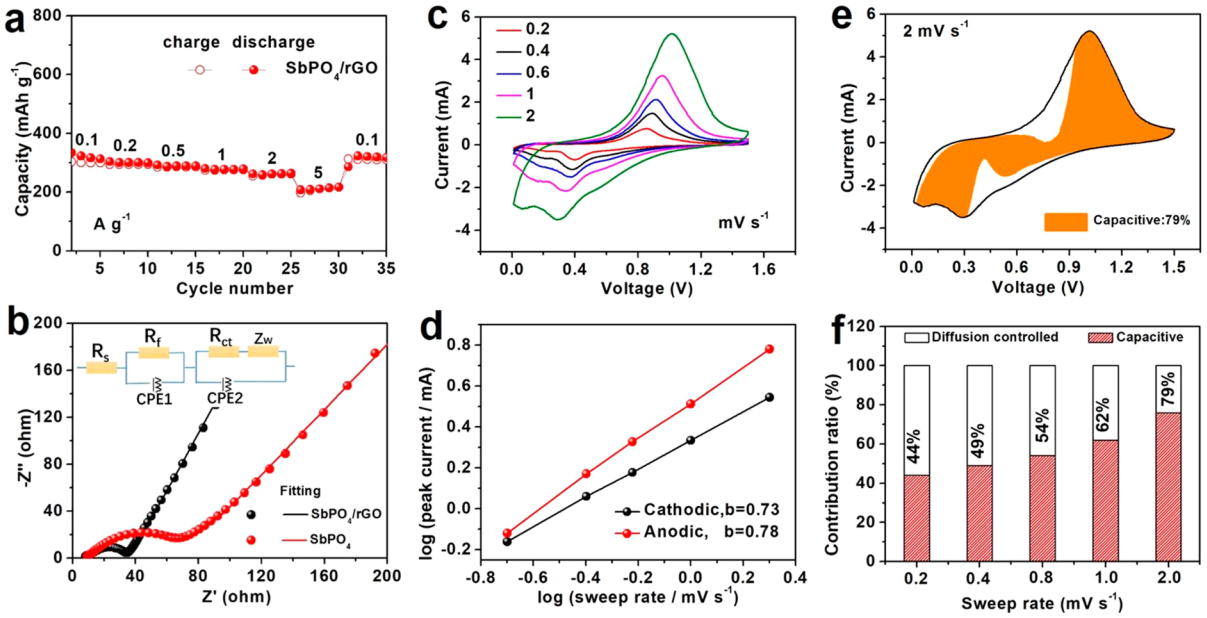

Figure 5. Kinetics analysis of Na storage mechanism. (a) Rate performance. (b) EIS spectra. (c) CV curves of $SbPO_4$/rGO at various scan rates. (d) Plots of log (scan rate) *versus* log (peak current). (e) Capacitive contribution in CV curves (shaded region) of $SbPO_4$/rGO. (f) Contribution ratio of capacitive capacity in $SbPO_4$/rGO at different sweep rates.

firmly attached to carbon, maintaining the electrochemical activity.

The excellent cycling performance can be attributed to the aggregation resistance of the Sb-containing particles, which comes from their secure attachment to rGO. First-principles calculations revealed that there are strong interactions at the interface region. Here, the (012) plane of Sb was adopted to simulate the contact surface of the particles. As revealed by our first-principles simulations, most of the contribution to the interaction between rGO and Sb come from van der Waals forces. The nature of such an interaction indicates that the bonding would not depend on the particular composition and termination of the Sb-containing particles. Therefore, we expect that the physical picture of the bonding patterns obtained on (012) planes can also be extended to other crystal facets including but not limited to (104) and (100) planes. Meanwhile, C−O groups were used as the anchor sites on rGO. More details about the computational model are described in Figures S16 and S17. Interestingly, even in the absence of the anchor sites, the binding energy of Sb (012) on rGO is ∼2.62 eV, which originates from the van der Waals interaction. Upon the involvement of the anchor sites, the binding energy further increases to 3.26 eV, owing to the chemical bonds between Sb and O/C atoms (Figure 4d). It is worth noting that the value of 3.26 eV is a lower limit because, in reality, the fluctuation of the rGO geometry is more flexible than that in the simulations, which could result in more effective bonding patterns. Overall, the van der Waals interactions lead to the deposition of the particles, and the formation of the chemical bonds effectively prevents these particles from diffusing and aggregating on rGO, both of which, cooperatively, stabilize the working units of the battery. This strong interaction is also supported by XPS spectra of $SbPO_4$ and $SbPO_4$/rGO discharged to 0.5 V, where Sb was *in situ* generated. Because Sb 3d is always interfered by O 1s, Sb 4d is used to confirm this point. As shown in Figure S18, Sb 4d of the discharged electrode from $SbPO_4$/rGO shifts to the high binding energies, as compared to that from $SbPO_4$. This shift indicates the decreasing of electron density around Sb, which is in good agreement with the interaction between Sb and rGO. Encouraged by these results, the long-term cycling of $SbPO_4$/rGO at a high rate was measured. As presented in Figure 4e, $SbPO_4$/rGO was cycled at 0.1 A g^{-1} for the first 10 cycles and then at 1 A g^{-1} for the following cycles. After 1000 cycles, the specific capacity still maintains at 100 mA h g^{-1}, corresponding to a capacity retention of 66%. Although this capacity is not impressive (Table S1), the lifespan outperforms many Sb-related anodes. Moreover, if evaluated in terms of the cycling stability, $SbPO_4$/rGO is also superior to many reports.

Figure 5a shows the rate performance of $SbPO_4$/rGO, where the specific capacity decreases from 323 mA h g^{-1} at 0.1 A g^{-1} to 301 mA h g^{-1} at 0.2 A g^{-1}, 289 mA h g^{-1} at 0.5 A g^{-1}, 278 mA h g^{-1} at 1 A g^{-1}, 262 mA h g^{-1} at 2 A g^{-1}, and 214 mA h g^{-1} at 5 A g^{-1}. Even at a high current density of 10 A g^{-1}, it still reaches 127 mA h g^{-1}. The capacity retention of $SbPO_4$/rGO is higher than that of $SbPO_4$ and most of the Sb-related materials (Figure S19). To gain insights about this result, EIS spectra were measured at 1.5 V after 10 cycles and fitted by an equivalent circuit (the inset of Figure 5b). R_s indicates the resistance of the electrolyte and cell components. R_f is the resistance related to the surface film; R_{ct} refers to the charge transfer resistance at the interfaces, and Z_w represents the Warburg impedance related to Na^+ diffusion.[22,36] It is noted that both R_f and R_{ct} of $SbPO_4$/rGO are much smaller than those of $SbPO_4$ (Table S2), implying the enhanced reaction kinetics in $SbPO_4$/rGO. Why $SbPO_4$/rGO shows the superior performances in rate capability and cycling stability could be illustrated as follows. First, rGO and as-formed Na_xSb and Sb offer three-dimensional highways for charge transfer and promote the electrochemical reactions.[37] Second, rGO and Na_3PO_4 work as the buffers to volume change upon cycling, improving the cycling stability. Third, the strong interaction between Sb and rGO restrains the particle pulverization and aggregation during sodiation/desodiation processes. All of

DOI: 10.1021/acsnano.8b08065
ACS Nano 2018, 12, 12869−12878

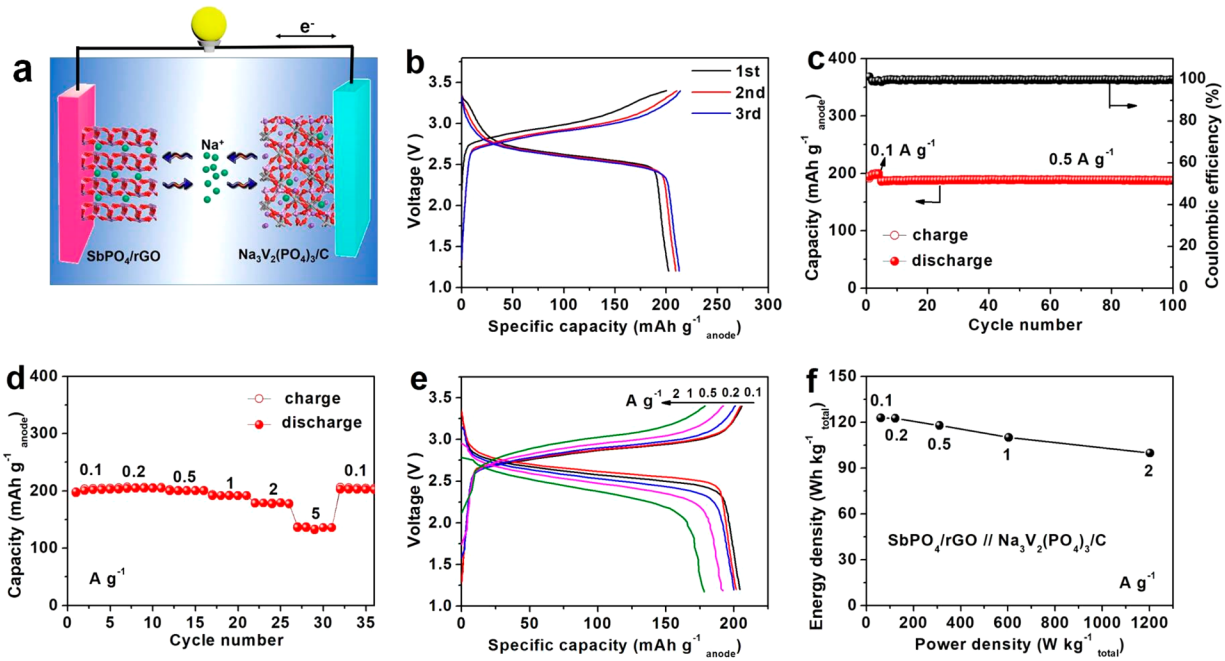

Figure 6. Electrochemical performances of the full cell ($SbPO_4$/rGO //$Na_3V_2(PO_4)_3$/C). (a) Scheme of the full cell. (b) Discharge/charge curves. (c) Cycling performance at 0.5 A g^{-1}. (d) Rate performance of the full cell. (e) Discharge/charge curves at different current density. Current density and specific capacity in (b−e) is calculated on the mass of the anode, $SbPO_4$/rGO. (f) Ragone-like plot of the full cell. Power density and energy density here are calculated on the total mass of the anode and cathode materials, $SbPO_4$/rGO + $Na_3V_2(PO_4)_3$/C.

these features make the composite promising as an anode material.

Kinetics analysis was conducted on the basis of CV curves at different scan rates. As shown in Figure 5c, these CV curves scanned from 0.2 to 2.0 mV s^{-1} exhibit a similar contour. The relationship between the peak current (i_p) and the scan rate (v) could be described by eq 3:[38]

$$i_p = av^b \tag{3}$$

where a and b are empirical constants that could be obtained by a logarithmic plot of i_p with v, as displayed in Figure 5d; b = 0.5 indicates an ideally diffusion-controlled electrochemical process, whereas b = 1.0 implies a typical surface-controlled electrochemical process. In most cases, b stays between 0.5 and 1.0, suggesting a mixed contribution from two processes. In $SbPO_4$/rGO, b values of the cathodic and anode peaks are identified as 0.73 and 0.78. According to Dunn *et al.*, the ratio of the two contributions could be estimated from eq 4:[39]

$$i = k_1v + k_2v^{1/2} \tag{4}$$

Here, i is the current at a fixed potential. k_1v and $k_2v^{1/2}$ represent the contributions of a surface-controlled process and a diffusion-controlled process, respectively. To simplify the calculation, this equation is reorganized by dividing both sides by $v^{1/2}$, giving eq 5:

$$i/v^{1/2} = k_1v^{1/2} + k_2 \tag{5}$$

In this context, k_1 and k_2 can be easily obtained as the slope and intercept point at the y-axis in a plot of $i/v^{1/2}$ *versus* $v^{1/2}$. Thus, the ratio of a diffusion-controlled process and a surface-controlled process at this potential could be clarified.[22,40] Expanding this procedure to other potentials would disclose the contributions of the two processes to the total capacity. As illustrated in Figure 5e, the capacitive process contributes 79% of the total capacity at a scan rate of 2.0 mV s^{-1}. These data gradually decrease to 44%, as the scan rate slows to 0.2 mV s^{-1} (Figure 5f).

In view of the excellent performances of $SbPO_4$/rGO in half cells, it is tested in full cells by using homemade $Na_3V_2(PO_4)_3$/C as a cathode material (Figure S20, Supporting Information).[41] Figure 6a shows the scheme of the full cell. The full cell was tested within 1.2−3.4 V at a current density of 0.5 A g^{-1}_{anode}. As shown in Figure 6b, there is a pronounced voltage plateau at 2.6 V, and this result would benefit the practical applications in the future. The cycling performances are evaluated at 0.5 A g^{-1}_{anode}, but the first five cycles were conducted at 0.1 A g^{-1}_{anode} for electrochemical activation. As illustrated in Figure 6c, the full cell displays a very stable cycling. After 100 cycles at 0.5 A g^{-1}, the capacity is still 190 mA h g^{-1}_{anode}, corresponding to a capacity retention of almost 99.2%. The superior rate performances of $SbPO_4$/rGO are also inherited in full cells (Figure 6d). There is a specific capacity of 204 mA h g^{-1}_{anode} for 0.1 A g^{-1}_{anode}, 202 mA h g^{-1}_{anode} for 0.2 A g^{-1}, 200 mA h g^{-1}_{anode} for 0.5 A g^{-1}_{anode}, 179 mA h g^{-1}_{anode} for 2 A g^{-1}_{anode}, and 136 mA h g^{-1}_{anode} for 5 A g^{-1}_{anode}. These results indicate that the full cells could be charged to 66.7% within 1.6 min. The electrode polarization slowly increases with the increasing rate (Figure 6e). Figure 6f shows the energy density and power density of full cells calculated on the basis of total mass of active materials ($Na_3V_2(PO_4)_3$/C + $SbPO_4$/rGO). It is found that the energy density decays slowly. Even at 1.2 kW kg^{-1}, there is still an energy density of 99.8 W h kg^{-1}_{total}, 81.3% of that at 0.06 kW kg^{-1}. All these data indicate the promising potential of $SbPO_4$/rGO as a high-performance anode material for Na ion batteries.

CONCLUSION

$SbPO_4$ nanorods are successfully deposited on reduce graphene oxide ($SbPO_4$/rGO) by a simple solvothermal

DOI: 10.1021/acsnano.8b08065
ACS Nano 2018, 12, 12869−12878

reaction, followed by a low-temperature annealing. A series of *ex/in situ* technologies confirm the stepwise alloying/dealloying of Sb to Na_3Sb over 0.01−1.5 V. The unique alignment of a layered structure makes the volume expansion preferentially occur along the transverse direction of $SbPO_4$ nanorods, as supported by *in situ* TEM images. $SbPO_4$/rGO presents a specific capacity of 323 mA h g^{-1} at 0.1 A g^{-1}. Even at 10 A g^{-1}, a capacity is still approximately ∼127 mA h g^{-1}. After 100 cycles at 0.5 A g^{-1}, the capacity retention remains at ∼99%, confirming the outstanding cycle stability. The superior performances could be attributed to rGO in the composite, which effectively enhances the electron conductivity, promotes the accommodation to volume change, and inhibits the potential peel-off of Sb. Inspired by these results, $SbPO_4$/rGO is evaluated in full cells by pairing with $Na_3V_2(PO_4)_3$/C. It works an average voltage at 2.6 V. After 100 cycles at 0.5 A g^{-1}, the capacity retention is kept at 99.2%. Even at 1.2 kW kg^{-1}_{total}, there is still an energy density of 99.8 W h kg^{-1}_{total}, making it attractive in the future.

EXPERIMENTAL SECTION

Material Synthesis. GO was fabricated using a modified Hummers method.[42] GO (30 mg) was dispersed in ethylene glycol (40 mL), followed by addition of $SbCl_3$ (228 mg) and $NH_4H_2PO_4$ (345 mg). This dispersion was heated to 70 °C and transferred to a Teflon-lined stainless autoclave. After being maintained at 160 °C for 4 h, the autoclave was cooled to room temperature naturally. The powders were collected by centrifuge, washed by distilled water and absolute ethanol, and dried at 60 °C overnight. Finally, the powders were annealed at 400 °C for 2 h in Ar/H_2 (95:5). This product, $SbPO_4$/rGO, was used for structure characterization and electrochemical performances. $SbPO_4$ nanoparticles were prepared without rGO in the recipe and used as the benchmark to illustrate the role of rGO.

Characterization. Powder XRD patterns were measured on an X-ray diffractometer (Bruker D8 Advanced, Germany), using monochromatic Cu Kα as a radiation source. SEM images were taken from a field-emission scanning electron microscope (Zeiss SUPRA55, Germany), connected with an energy-dispersive X-ray spectrometer (Oxford Instruments). TEM images were acquired on an aberration-corrected transmission electron microscope (FEI Titan Themis G2, USA) operated at 300 kV. Raman spectra were obtained on a LabRAM HR800 Raman spectrometer, using an excitation at 632 nm at room temperature. XPS spectra were achieved from an X-ray photoelectron spectrometer (ESCA LAB 250, USA). TGA was conducted on a thermal analyzer (Mettler Toledo TGA/SDTA85, Canada) from room temperature to 800 °C in air. N_2 sorption isotherms were measured on a gas sorptometer (Micromeritics ASAP 2020 HD88, USA) at 77 K.

Electrochemical Measurements. Electrochemical performances of $SbPO_4$ and $SbPO_4$/rGO as anode materials in sodium ion batteries were evaluated in CR2032-type coin cells, using pure sodium foil as the counter electrode and glass fitter (whatman GF/F) as a separator. The working electrode was fabricated by spreading a slurry of $SbPO_4$ or $SbPO_4$/rGO, acetylene black, and sodium alginate (SA) in a weight ratio of 7:2:1 on a copper foil. After the foil was dried in vacuum at 60 °C for 12 h, the electrode was cut into disks with diameters of 12 nm. The mass loading of active material was 1.0−1.5 mg cm^{-2}. Then, the coin cells were assembled in an argon-filled glovebox (Mikrouna, Super 1220/750/900, H_2O < 1 ppm, O_2 < 1 ppm), using 1.0 M $NaClO_4$ in propylene carbonate containing 3 wt % FEC as an electrolyte. For full cells, the cathode was made of homemade $Na_3V_2(PO_4)_3$/C, acetylene black, and poly(vinylidene) in a weight ratio of 8:1:1 deposited on an alumium foil. The anode was fabricated by the above protocol and electrochemically activated in a half cell before it was assembled into full cells. The capacity ratio between anode and cathode was controlled to about 1.2:1. In this case, the anode capacity slightly exceeds the cathode one, promoting the utilization of cathode materials and preventing the formation of dendrites. CVs were performed using an electrochemical workstation (LK 2005A, China) at room temperature. Galvanostatic discharge/charge profiles were obtained on battery cyclers (LAND CT-2001A, China) between 0.01 and 1.5 V at 25 °C. EIS spectra were taken on an electrochemical workstation (Autolab PGSTAT 302N) over a frequency range of 100 kHz to 0.01 Hz.

***In Situ* TEM Characterization.** *In situ* TEM images and SAED patterns were obtained out using Tecnai F20 at 200 kV equipped with an OneView IS (Gatan) camera. The *in situ* experiment was conducted using a simplified battery configuration with $SbPO_4$ dispersed onto a half-copper mesh as the working electrode and a piezo-driven tungsten tip coated by Na as the counter electrode. To achieve this fabrication, $SbPO_4$ was dispersed in a half-copper grid and transferred to a specially designed specimen holder (PicoFemto). Then, the W tip was used to scratch the surface of Na metal. All of the process was conducted in an argon-filled glovebox. Finally, the holder was transferred into a microscope column. During the transfer process, the Na was shortly exposed to the air to form a layer of Na_xO on the surface of Na, serving as the solid electrolyte. The W tip is kept in touch with $SbPO_4$ by a piezo-ceramic manipulator. To initialize the sodiation, a bias of −2 V was applied on $SbPO_4$ against the counter electrode to promote Na ion transport through the Na_2O layer.

Computation Details. All calculations were performed using the Vienna ab initio simulation package (VASP).[43,44] The energy cutoff for the plane-wave basis set was 400 eV, and optB86b-vdW was employed as the exchange-correlation functional.[45,46] All atoms were allowed to relax until the maximum force was below 0.03 Å /eV. Dipole correction on the total energies was added along the perpendicular direction.

ASSOCIATED CONTENT

Supporting Information

The Supporting Information is available free of charge on the ACS Publications website at DOI: 10.1021/acsnano.8b08065.

Raman and EDX spectra, TGA curve, XRD patterns, XPS spectrum, SEM and TEM images, N_2 sorption isotherms, *ex situ* SAED patterns and HRTEM images, charge/discharge profiles and cycling performance, unit cells and rGO model, EIS data (PDF)

Movie S1: Sodium insertion in $SbPO_4$ nanostructures recorded at low magnification (AVI)

Movie S2: Sodium insertion in $SbPO_4$ nanostructures recorded by at selected area electron diffraction (AVI)

AUTHOR INFORMATION

Corresponding Authors

*E-mail: p-gao@pku.edu.cn.

*E-mail: yangjian@sdu.edu.cn.

ORCID

Jun Pan: 0000-0001-8593-271X

Qiang Fu: 0000-0002-6682-8527

Peng Gao: 0000-0003-0860-5525

Jian Yang: 0000-0002-6401-276X

Author Contributions

⊥J.P. and S.C. contributed equally to this work.

Notes

The authors declare no competing financial interest.

ACKNOWLEDGMENTS

The authors want to thank the National Nature Science Foundation of China (Nos. 21471090, 61527809, 51172076, 51502007, and 51672007), Taishan Scholarship in Shandong

DOI: 10.1021/acsnano.8b08065
ACS Nano 2018, 12, 12869−12878

Provinces (No. ts201511004), Development Programs of Shandong Province (2017GGX40101 and 2017CXGC0503), the Fundamental Research Funds of Shandong University (2018JC023), and "2011 Program" Peking-Tsinghua-IOP Collaborative Innovation Center of Quantum Matter for financial support. The authors acknowledge Electron Microscopy Laboratory in Peking University for the use of Cs-corrected electron microscope and the *in situ* TEM platform. Theoretical calculation in this work was performed on the HPC Cloud Platform of Shandong University. We also thank Mr. Zhenjie Chen in Suzhou Institute of Nano-Tech and Nano-Bionics, Chinese Academy of Sciences, for *in situ* XRD patterns.

REFERENCES

(1) Gogotsi, Y.; Simon, P. True Performance Metrics in Electrochemical Energy Storage. *Science* **2011**, *334*, 917−918.

(2) Han, J. W.; Kong, D. B.; Lv, W.; Tang, D. M.; Han, D. L.; Zhang, C.; Liu, D. H.; Xiao, Z. C.; Zhang, X. H.; Xiao, J.; He, X. Z.; Hsia, F. C.; Zhang, C.; Tao, Y.; Golberg, D.; Kang, F. Y.; Zhi, L. J.; Yang, Q. H. Caging Tin Oxide in Three-Dimensional Graphene Networks for Superior Volumetric Lithium Storage. *Nat. Commun.* **2018**, *9*, 402.

(3) Ji, L. W.; Zhou, W. D.; Chabot, V.; Yu, A. P.; Xiao, X. C. Reduced Graphene Oxide/Tin−Antimony Nanocomposites as Anode Materials for Advanced Sodium-Ion Batteries. *ACS Appl. Mater. Interfaces* **2015**, *7*, 24895−24901.

(4) Tian, W. F.; Zhang, S. L.; Huo, C. X.; Zhu, D. M.; Li, Q. W.; Wang, L.; Ren, X. C.; Xie, L.; Guo, S. Y.; Chu, P. K.; Zeng, H. B.; Huo, K. F. Few-Layer Antimonene: Anisotropic Expansionand Reversible Crystalline-Phase Evolution Enable Large-Capacity and Long-Life Na-Ion Batteries. *ACS Nano* **2018**, *12*, 1887−1893.

(5) Xiao, L. F.; Cao, Y. L.; Henderson, W. A.; Sushko, M. L.; Shao, Y. Y.; Xiao, J.; Wang, W.; Engelhard, M. H.; Nie, Z. M.; Liu, J. Hard Carbon Nanoparticles as High-Capacity, High-Stability Anodic Materials for Na-Ion Batteries. *Nano Energy* **2016**, *19*, 279−288.

(6) Jin, J.; Yu, B. J.; Shi, Z. Q.; Wang, C. Y.; Chong, C. B. Lignin-Based Electrospun Carbon Nanofibrous Webs as Free-Standing and Binder-Free Electrodes for Sodium Ion Batteries. *J. Power Sources* **2014**, *272*, 800−807.

(7) Cao, Y. L.; Xiao, L. F.; Sushko, M. L.; Wang, W.; Schwenzer, B.; Xiao, J.; Nie, Z. M.; Saraf, L. V.; Yang, Z. G.; Liu, J. Sodium Ion Insertion in Hollow Carbon Nanowires for Battery Applications. *Nano Lett.* **2012**, *12*, 3783−3787.

(8) Lee, S. H.; Yu, S. H.; Lee, J. E.; Jin, A. H.; Lee, D. J.; Lee, N.; Jo, H. Y.; Shin, K.; AHN, T. Y.; Kim, Y. W.; Choe, H.; Sung, Y. E.; Hyeon, T. Self-Assembled Fe_3O_4 Nanoparticle Clusters as High-Performance Anodes for Lithium Ion Batteries *via* Geometric Confinement. *Nano Lett.* **2013**, *13*, 4249−4256.

(9) Liu, X.; Zhang, K.; Lei, K. X.; Li, F. J.; Tao, Z. L.; Chen, J. Facile Synthesis and Electrochemical Sodium Storage of CoS_2 Micro/Nano-Structures. *Nano Res.* **2016**, *9*, 198−206.

(10) Walter, M.; Erni, R.; Kovalenko, M. V. Inexpensive Antimony Nanocrystals and Their Composites with Red Phosphorus as High-Performance Anode Materials for Na-Ion Batteries. *Sci. Rep.* **2015**, *5*, 8418.

(11) Zheng, Y.; Zhou, T. F.; Zhang, C. F.; Mao, J. F.; Liu, H. K.; Guo, Z. P. Boosted Charge Transfer in SnS/SnO_2 Heterostructures: Toward High Rate Capability for Sodium-Ion Batteries. *Angew. Chem., Int. Ed.* **2016**, *55*, 3408−3413.

(12) Cho, E.; Song, K.; Park, M. H.; Nam, K. W.; Kang, Y. M. SnS 3D Flowers with Superb Kinetic Properties for Anodic Use in Next-Generation Sodium Rechargeable Batteries. *Small* **2016**, *12*, 2510−2517.

(13) Yu, D. Y. W.; Prikhodchenko, P. V.; Mason, C. W.; Batabyal, S. K.; Gun, J.; Sladkevich, S.; Medvedev, A. G.; Lev, O. High-Capacity Antimony Sulphide Nanoparticle-Decorated Graphene Composite as Anode for Sodium-Ion Batteries. *Nat. Commun.* **2013**, *4*, 2922.

(14) Xiong, X. H.; Wang, G. H.; Lin, Y. W.; Wang, Y.; Ou, X.; Zheng, F. H.; Yang, C. H.; Wang, J. H.; Liu, M. L. Enhancing Sodium Ion Battery Performance by Strongly Binding Nanostructured Sb_2S_3 on Sulfur-Doped Graphene Sheets. *ACS Nano* **2016**, *10*, 10953−10959.

(15) Zhang, Y. D.; Zhu, P. Y.; Huang, L. L.; Xie, J.; Zhang, S. C.; Cao, G. S.; Zhao, X. B. Few-Layered SnS_2 on Few-Layered Reduced Graphene Oxide as Na-Ion Battery Anode with Ultralong Cycle Life and Superior Rate Capability. *Adv. Funct. Mater.* **2015**, *25*, 481−489.

(16) Yang, X.; Zhang, R. Y.; Zhao, J.; Wei, Z. X.; Wang, D. X.; Bie, X. F.; Gao, Y.; Wang, J.; Du, F.; Chen, G. Amorphous Tin-Based Composite Oxide: A High-Rate and Ultralong-Life Sodium-Ion-Storage Material. *Adv. Energy Mater.* **2018**, *8*, 1701827.

(17) Hu, P.; Ma, J.; Wang, T. S.; Qin, S. S.; Zhang, C. J.; Shang, C. Q.; Zhao, J. H.; Cui, G. L. NASICON-Structured $NaSn_2(PO_4)_3$ with Excellent High-Rate Properties as Anode Material for Lithium Ion Batteries. *Chem. Mater.* **2015**, *27*, 6668−6674.

(18) Behm, M.; Irvine, J. T. S. Influence of Structure and Composition upon Performance of Tin Phosphate Based Negative Electrodes for Lithium Batteries. *Electrochim. Acta* **2002**, *47*, 1727−1738.

(19) Yin, W. G.; Liu, J. J.; Duan, C. G.; Mei, W. N.; Smith, R. W.; Hardy, J. R. Superionicity in Na_3PO_4: A Molecular Dynamics Simulation. *Phys. Rev. B: Condens. Matter Mater. Phys.* **2004**, *70*, 064302.

(20) Liu, Y. C.; Zhang, N.; Jiao, L. F.; Tao, Z. L.; Chen, J. Ultrasmall Sn Nanoparticles Embedded in Carbon as High-Performance Anode for Sodium-Ion Batteries. *Adv. Funct. Mater.* **2015**, *25*, 214−220.

(21) Yi, Z.; Han, Q. G.; Zan, P.; Wu, Y. M.; Cheng, Y.; Wang, L. M. Sb Nanoparticles Encapsulated into Porous Carbon Matrixes for High-Performance Lithium-Ion Battery Anodes. *J. Power Sources* **2016**, *331*, 16−21.

(22) Niu, F. E.; Yang, J.; Wang, N. N.; Zhang, D. P.; Fan, W. L.; Yang, J.; Qian, Y. T. $MoSe_2$-Covered N, P-Doped Carbon Nanosheets as a Long-Life and High-Rate Anode Material for Sodium-Ion Batteries. *Adv. Funct. Mater.* **2017**, *27*, 1700522.

(23) Ramireddy, T.; Sharma, N.; Xing, T.; Chen, Y.; Leforestier, J.; Glushenkov, A. M. Size and Composition Effects in Sb-Carbon Nanocomposites for Sodium-Ion Batteries. *ACS Appl. Mater. Interfaces* **2016**, *8*, 30152−30164.

(24) Wang, N. N.; Bai, Z. C.; Qian, Y. T.; Yang, J. One-Dimensional Yolk-Shell Sb@Ti-O-P Nanostructures as a High-Capacity and High-Rate Anode Material for Sodium Ion Batteries. *ACS Appl. Mater. Interfaces* **2017**, *9*, 447−454.

(25) Zhang, C.; Wang, X.; Liang, Q. F.; Liu, X. Z.; Weng, Q. H.; Liu, J. W.; Yang, Y. J.; Dai, Z. H.; Ding, K. J.; Bando, Y.; Tang, J.; Golberg, D. Amorphous Phosphorus/Nitrogen-Doped Graphene Paper for Ultrastable Sodium-Ion Batteries. *Nano Lett.* **2016**, *16*, 2054−2060.

(26) Ou, X.; Yang, C. H.; Xiong, X. H.; Zheng, F. H.; Pan, Q. C.; Jin, C.; Liu, M. L.; Huang, K. V. A New rGO-Overcoated Sb_2Se_3 Nanorods Anode for Na^+ Battery: *In Situ* X-Ray Diffraction Study on a Live Sodiation/Desodiation Process. *Adv. Funct. Mater.* **2017**, *27*, 1606242.

(27) Hou, H. S.; Jing, M. J.; Huang, Z. D.; Yang, Y. C.; Zhang, Y.; Chen, J.; Wu, Z. B.; Ji, X. B. One-Dimensional Rod-Like Sb_2S_3 Based Anode for High-Performance Sodium-Ion Batteries. *ACS Appl. Mater. Interfaces* **2015**, *7*, 19362−19369.

(28) Chen, S. L.; Wang, L. P.; Shao, R. W.; Zou, J.; Cai, R.; Lin, J. H.; Zhu, C. Y.; Zhang, J. M.; Xu, F.; Cao, J.; Feng, J. C.; Qi, J. L.; Gao, P. Atomic Structure and Migration Dynamics of MoS_2/Li_xMoS_2 Interface. *Nano Energy* **2018**, *48*, 560−568.

(29) Gao, P.; Wang, L. P.; Zhang, Y. Y.; Huang, Y.; Liu, K. H. Atomic-Scale Probing of the Dynamics of Sodium Transport and Intercalation-Induced Phase Transformations in MoS_2. *ACS Nano* **2015**, *9*, 11296−11301.

(30) Soto, F. A.; Yan, P. F.; Engelhard, M. H.; Marzouk, A.; Wang, C. M.; Xu, G. L.; Chen, Z. H.; Amine, K.; Liu, J.; Sprenkle, V. L.; El-Mellouhi, F.; Balbuena, P. B.; Li, X. L. Tuning the Solid Electrolyte

DOI: 10.1021/acsnano.8b08065
ACS Nano 2018, 12, 12869−12878

Interphase for Selective Li-and Na-Ion Storage in Hard Carbon. *Adv. Mater.* **2017**, *29*, 1606860.
(31) Yang, C. L.; Li, W. H.; Yang, Z. Z.; Gu, L.; Yu, Y. Nanoconfined Antimony in Sulfur and Nitrogen Co-Doped Three-Dimensionally (3D) Interconnected Macroporous Carbon for High-Performance Sodium-Ion Batteries. *Nano Energy* **2015**, *18*, 12−19.
(32) Darwiche, A.; Marino, C.; Sougrati, M. T.; Fraisse, B.; Stievano, L.; Monconduit, L. Better Cycling Performances of Bulk Sb in Na-Ion Batteries Compared to Li-Ion Systems: An Unexpected Electrochemical Mechanism. *J. Am. Chem. Soc.* **2012**, *134*, 20805−20811.
(33) He, M.; Kravchyk, K.; Walter, M.; Kovalenko, M. V. Monodisperse Antimony Nanocrystals for High-Rate Li-Ion and Na-Ion Battery Anodes: Nano *versus* Bulk. *Nano Lett.* **2014**, *14*, 1255−1262.
(34) Ji, L. W.; Gu, M.; Shao, Y. Y.; Li, X. L.; Engelhard, M. H.; Arey, B. W.; Wang, W.; Nie, Z. M.; Xiao, J.; Wang, C. M.; Zhang, J. G.; Liu, J. Controlling SEI Formation on SnSb-Porous Carbon Nanofibers for Improved Na Ion Storage. *Adv. Mater.* **2014**, *26*, 2901−2908.
(35) Zhao, J.; Lee, H. W.; Sun, J.; Yan, K.; Liu, Y. Y.; Liu, W.; Lu, Z.; Lin, D. C.; Zhou, Z. M.; Cui, Y. Metallurgically Lithiated SiO_x Anode with High Capacity and Ambient Air Compatibility. *Proc. Natl. Acad. Sci. U. S. A.* **2016**, *113*, 7408−7413.
(36) Pan, J.; Wang, N. N.; Zhou, Y. L.; Yang, X. F.; Zhou, W. Y.; Qian, Y. T.; Yang, J. Simple Synthesis of a Porous Sb/Sb_2O_3 Nanocomposite for a High-Capacity Anode Material in Na-Ion Batteries. *Nano Res.* **2017**, *10*, 1794−1803.
(37) Cole, R. S.; Frech, R. Characterization of The Sodium Sulfate-Sodium Phosphate System. *J. Mol. Struct.* **2002**, *643*, 101−107.
(38) Augustyn, V.; Come, J.; Lowe, M. A.; Kim, J. W.; Taberna, P. L.; Tolbert, S. H.; Abruna, H. D.; Simon, P.; Dunn, B. High-Rate Electrochemical Energy Storage Through Li^C Intercalation Pseudocapacitance. *Nat. Mater.* **2013**, *12*, 518−522.
(39) Brezesinski, T.; Wang, J.; Polleux, J.; Dunn, B.; Tolbert, S. H. Templated Nanocrystal-Based Porous TiO_2 Films for Next-Generation Electrochemical Capacitors. *J. Am. Chem. Soc.* **2009**, *131*, 1802−1809.
(40) Chao, D. L.; Zhu, C. R.; Yang, P. H.; Xia, X. H.; Liu, J. L.; Wang, J.; Fan, X. F.; Savilov, S. V.; Lin, J. Y.; Fan, H. J.; Shen, Z. X. Array of Nanosheets Render Ultrafast and High-Capacity Na-Ion Storage by Tunable Pseudocapacitance. *Nat. Commun.* **2016**, *7*, 12122.
(41) Li, G. Q.; Jiang, D. L.; Wang, H.; Lan, X. Z.; Zhong, H. H.; Jiang, Y. Glucose-Assisted Synthesis of $Na_3V_2(PO_4)/C$ Composite as an Electrode Material for High-Performance Sodium-Ion Batteries. *J. Power Sources* **2014**, *265*, 325−334.
(42) Hummers, W.; Offeman, R. Preparation of Graphitic Oxide. *J. Am. Chem. Soc.* **1958**, *80*, 1339−1339.
(43) Kresse, G.; FurthmÜLler, J. Efficiency of Ab-Initio Total Energy Calculations for Metals and Semiconductors Using a Plane-Wave Basis Set. *Comput. Mater. Sci.* **1996**, *6*, 15−50.
(44) Kresse, G.; FurthmÜLler, J. Efficient Iterative Schemes for Ab Initio Total-Energy Calculations Using a Plane-Wave Basis Set. *Phys. Rev. B: Condens. Matter Mater. Phys.* **1996**, *54*, 11169−11186.
(45) Dion, M.; Rydberg, H.; Schröder, E.; Langreth, D. C.; Lundqvist, B. I. Van Der Waals Density Functional for General Geometries. *Phys. Rev. Lett.* **2004**, *92*, 246401.
(46) Klimeš, J.; Bowler, D. R.; Michaelides, A. Chemical Accuracy for the Van Der Waals Density Functional. *J. Phys.: Condens. Matter* **2010**, *22*, 022201.

DOI: 10.1021/acsnano.8b08065
ACS Nano 2018, 12, 12869−12878